

# An Exceptionally Mild and Scalable Solution-Phase Synthesis of Molybdenum Carbide Nanoparticles for Thermocatalytic CO<sub>2</sub> **Hydrogenation**

Frederick G. Baddour,\*\*,†® Emily J. Roberts,‡ Anh T. To,† Lu Wang,<sup>§®</sup> Susan E. Habas,† Daniel A. Ruddy, \*\* Nicholas M. Bedford, \*\* Joshua Wright, \*\* Connor P. Nash, \*\* Joshua A. Schaidle, \*\* Onnor P. Nash, \*\* Onnor P. Onnor P. Nash, \*\* Onnor P. Onno Richard L. Brutchey,\*,\*,\* and Noah Malmstadt\*,\*,\$,#

Supporting Information

ABSTRACT: Transition metal carbides (TMCs) have demonstrated outstanding potential for utilization in a wide range of catalytic applications because of their inherent multifunctionality and tunable composition. However, the harsh conditions required to prepare these materials have limited the scope of synthetic control over their physical properties. The development of low-temperature, carburization-free routes to prepare TMCs would unlock the versatility of this class of materials, enhance our understanding of their physical properties, and enable their cost-effective production at industrial scales. Here, we report an exceptionally mild and



scalable solution-phase synthesis route to phase-pure molybdenum carbide  $(\alpha - MoC_{1-x})$  nanoparticles (NPs) in a continuous flow millifluidic reactor. We exploit the thermolytic decomposition of  $Mo(CO)_6$  in the presence of a surface-stabilizing ligand and a high boiling point solvent to yield  $MoC_{1-x}$  NPs that are colloidally stable and resistant to bulk oxidation in air. To demonstrate the utility of this synthetic route to prepare catalytically active TMC NPs, we evaluated the thermochemical CO<sub>2</sub> hydrogenation performance of  $\alpha$ -MoC<sub>1-x</sub> NPs dispersed on an inert carbon support. The  $\alpha$ -MoC<sub>1-x</sub>/C catalyst exhibited a 2fold increase in both activity on a per-site basis and selectivity to  $C_{2+}$  products as compared to the bulk  $\alpha$ -Mo $C_{1-x}$  analogue.

#### INTRODUCTION

In recent years, transition metal carbides (TMCs) have garnered significant research attention due to their excellent catalytic performance for a wide range of transformations including  ${\rm CO_2}$  reduction, ammonia synthesis, and hydrodeoxygenation reactions. <sup>1–3</sup> In particular, TMCs have been identified as potential low-cost candidates for CO2 reduction because of their multifunctionality that enables H<sub>2</sub> dissociation, C=O bond scission, and reducible-oxide-like behavior, all of which are crucial to the conversion of CO2 to CO and higher hydrocarbons. In addition to this multifunctionality (i.e., metallic sites, acidic sites, and basic sites), TMCs have been found to exhibit noble-metal-like behavior, resist sintering, and offer opportunities to tune catalytic reactivity based on the selection of metal, stoichiometry, and crystal structure.<sup>4,5</sup>

Solution-phase synthetic methods to prepare colloidal nanoparticles (NPs) of noble metals have been extensively developed over the past 20 years to control composition, size, and morphology, which has resulted in improved catalytic performance (e.g., activity and selectivity) and facilitated the understanding of key structure-reactivity relationships that have driven the development of next-generation catalytic NPs with tailored performance.<sup>6</sup> Unfortunately, there are comparatively few techniques in the synthetic toolbox that afford the same degree of control over the physical properties of TMCs.

Received: October 18, 2019 Published: January 2, 2020



<sup>&</sup>lt;sup>†</sup>National Bioenergy Center, National Renewable Energy Laboratory, 15013 Denver West Parkway, Golden, Colorado 80401-3305, United States

<sup>&</sup>lt;sup>‡</sup>Department of Chemistry, University of Southern California, 840 Downey Way, Los Angeles, California 90089-0744, United States §Mork Family Department of Chemical Engineering and Materials Science, University of Southern California, 925 Bloom Walk, Los Angeles, California 90089-1211, United States

School of Chemical Engineering, University of New South Wales, High Street, Sydney, New South Wales 2052, Australia

<sup>&</sup>lt;sup>1</sup>Department of Physics, Illinois Institute of Technology, 3101 South Dearborn Street, Chicago, Illinois 60616, United States

 $<sup>^{\#}</sup>$ Department of Biomedical Engineering, University of Southern California, 1042 Downey Way, Los Angeles, California 90089-0260, United States

The realization of a solution-based synthetic methodology for TMCs represents a significant challenge, as, in general, these materials are prepared by the carburization of a metal, metal oxide, or metal nitride with a carbon source (e.g., activated carbon, CH<sub>4</sub>, and light alkanes) in H<sub>2</sub> at temperatures typically above 600 °C to form polycrystalline porous solids. To date, only Ni and Fe carbide NPs have been synthesized in solution at comparatively mild temperatures. 7-14 Notably, group 6 TMCs with catalytic relevance to CO<sub>2</sub> hydrogenation are even less well studied, with only one example of nanometer-sized powder of the cubic phase  $\alpha$ -MoC<sub>1-x</sub> produced by the sonochemical decomposition of Mo(CO)6 that still relies on a high-temperature carburization step. Only recently have researchers been able to controllably synthesize nanostructured TMCs employing metal organic frameworks (MOFs), 16 resins, 17 or other porous materials as templates<sup>18</sup> or temporary scaffolds to attain free-standing nanoparticles. 19 While these methodologies constitute significant advancements in the nanostructuring of TMCs, the dependence of these syntheses on high temperatures and complex methodologies still limit the spectrum of accessible features and the scalability of these methods. Therefore, the development of mild and versatile solution-phase routes to synthesize TMC NPs is required to enhance the understanding of the physical properties of these materials and enable their cost-effective synthesis at industrially relevant scales.

In contrast to traditional batch reactions commonly used to prepare colloidal NPs, continuous flow millifluidic (mF) synthesis has been identified as an alternative approach for the large-scale production of NP materials that mitigates many of the limitations of batch methods.<sup>20</sup> For example, simple volumetric scaling of batch reactions often leads to inhomogeneities resulting from changes in mass and thermal transport that can lead to significant batch-to-batch variability because of altered nucleation and growth rates.<sup>21</sup> The resulting changes to particle features may negatively impact the catalytic properties of the resultant NPs and may ultimately render volumetric scaling unsuitable for the production of large quantities of NPs with controlled physical attributes.<sup>22</sup> Continuous flow mF synthesis approaches, however, can reliably produce particles with well-controlled sizes and can be prepared with increased yields due to the superior heat and mass transport properties afforded by the high surface-area-tovolume ratios that are intrinsic to confined micrometer-scale channels. These methods are amenable to process intensification and automation, which increase throughput and fidelity. Moreover, the development of continuous flow methods to prepare colloidal NPs in quantities on the order of grams per channel enables both the fundamental evaluation of their physical properties and catalytic performance while demonstrating the scalability of their production.<sup>25</sup>

Herein, we report an exceptionally mild and scalable solution-phase synthesis route to phase-pure molybdenum carbide ( $\alpha$ -MoC<sub>1-x</sub>) NPs in a continuous flow mF reactor. The MoC<sub>1-x</sub> NPs (NP-MoC<sub>1-x</sub>) are colloidally stable and protected from uncontrolled bulk oxidation by organic ligands. The synthesized MoC<sub>1-x</sub> NPs were dispersed on an inert carbon support and evaluated for thermochemical CO<sub>2</sub> hydrogenation after activation in H<sub>2</sub>. The resulting NP-MoC<sub>1-x</sub>/C catalyst exhibited site-time yields and C<sub>2+</sub> selectivities 2-fold higher than those of the bulk  $\alpha$ -MoC<sub>1-x</sub> analogues and site-time yields an order of magnitude greater than a traditional Fischer–Tropsch catalyst (i.e., Fe/ $\gamma$ -Al<sub>2</sub>O<sub>3</sub>)

for the conversion of CO<sub>2</sub>. The scalable and highly versatile solution-phase synthesis strategy presented herein demonstrates that these methods can be applied to the production of colloidally stable group 6 TMCs and opens the door to a better understanding and greater control over the catalytically important features of this class of materials.

#### EXPERIMENTAL SECTION

**General.** Synthetic manipulations to prepare α-MoC<sub>1-x</sub> nanoparticles were conducted under a  $N_2$  atmosphere using standard Schlenk techniques or in a  $N_2$ -filled Vacuum Atmospheres glovebox, unless otherwise noted. Oleylamine (OAm, 70% technical grade) and 1-octadecene (ODE, 90%) were purchased from Sigma-Aldrich and dried prior to use by heating to 120 °C under vacuum for ≥5 h and stored in an  $N_2$ -filled glovebox prior to use. Molybdenum hexacarbonyl (98%) was purchased from Strem Chemicals and used as received. The carbon support (Vulcan XC 72R) was supplied by Cabot and used as received.

Continuous Flow Synthesis of  $\alpha\text{-MoC}_{1-x}$  NPs. The glass millifluidic (mF) reactor was equilibrated at 320 °C overnight and prepressurized to 40 psig with N2 prior to each synthesis. A precursor solution (625 mM) was prepared by mixing a portion of Mo(CO)<sub>6</sub> (6.336 g, 24 mmol) with OAm (31.2 mL, 94.82 mmol) and ODE (7.2 mL) and heating the mixture to 140 °C for 1 h under N<sub>2</sub>. The solution was cooled to 100 °C, then transferred to a glass syringe fitted with heat tape maintained at 80 °C to maintain a homogeneous solution. The glass syringe was then fastened to a syringe pump and connected to the inlet tubing of the mF reactor. The Mo(CO)<sub>6</sub> precursor solution was injected at a constant flow rate of 12 mL h<sup>-1</sup> The  $\alpha$ -MoC<sub>1-x</sub> NP product was directed past an in-line flow sensor (set to record every 0.1 s) and was collected at the reactor outlet. The mass flow rate of the product mixture was recorded with an analytical balance, and excess pressure was relieved through a 40 psigbackpressure regulator. The resulting  $\alpha\text{-MoC}_{1-x}$  NP suspension was combined with hexanes in a 1:5 (v/v) ratio of hexanes/reaction mixture, before being transferred into six 50 mL centrifuge tubes. The mixture was vortex mixed for 30 s, bath sonicated for 5 min, and then precipitated by adding a portion of ethanol (34 mL) to each centrifuge tube. The ethanolic product mixture was briefly sonicated, and then the  $\alpha$ -MoC<sub>1-x</sub> NPs were collected by centrifugation (6000 rpm, 10 min). The colorless supernatant was decanted and discarded, and the black nanoparticle pellet was redispersed by adding 2 mL of CHCl<sub>3</sub> to each centrifuge tube. The NPs were washed by precipitating the NPs an additional time with ethanol (38 mL per tube) followed by sonication and centrifugation (6000 rpm, 10 min) to isolate the product. The resulting  $\alpha$ -MoC $_{1-x}$  NPs were dispersed in CHCl $_3$  to achieve a suspension of ca. 5 mg mL<sup>-1</sup> for subsequent supporting on

Synthesis of Carbon-Supported NPs. The NPs recovered following centrifugation were redispersed in ca. 5 mL of CHCl $_3$  and added dropwise to a rapidly stirring suspension of Vulcan XC 72R carbon dispersed in ca. 50 mL of CHCl $_3$  to yield a catalyst of 3.66 wt % Mo loading. The mixture was sonicated for 5 min and stirred overnight. The resulting catalyst was separated via centrifugation at 8000 rpm for 10 min, dried in vacuo, and stored in an N $_2$ -filled glovebox prior to catalytic evaluation.

**Characterization.** Powder X-ray diffraction (XRD) data were collected using a Rigaku Ultima IV diffractometer with a Cu  $K\alpha$  source (40 kV, 44 mA). Diffraction patterns were collected in the  $2\theta$  range of  $20-80^{\circ}$  at a scan rate of  $4^{\circ}$  min<sup>-1</sup>. XRD samples were prepared by drop-casting a CHCl<sub>3</sub> suspension of unsupported NPs onto a glass sample holder. Diffraction patterns were compared to powder diffraction files from the International Centre for Diffraction Data (ICDD). The crystallite sizes were calculated from XRD peak broadening of the unsupported catalysts using the Scherrer equation. Samples for transmission electron microscopy (TEM) were drop-cast onto carbon-coated copper grids (Ted Pella part no. 01824) from CHCl<sub>3</sub> suspensions. Imaging was performed using a FEI Technai G2 ST30 TEM operating at 300 kV or a JEOL JEM2100F microscope

operating at 200 kV. All image analysis was conducted with ImageJ software. <sup>26</sup> Lattice spacings were measured from the fast-Fourier transforms of high-resolution TEM (HRTEM) images. Size distributions were determined from a manual measurement of >100 of the isolated crystalline domains of the multipodal NPs. Metal loadings were determined by inductively coupled plasma optical emission spectroscopy (ICP-OES) performed by Galbraith Laboratories (Knoxville, TN). X-ray photoelectron spectroscopy (XPS) data were acquired on a Kratos Axis Ultra X-ray photoelectron spectrometer with the analyzer lens in hybrid mode. High-resolution scans were performed using a monochromatic aluminum anode with an operating current of 5 mA and voltage of 10 kV using a step size of 0.1 eV, a pass energy of 20 eV, and a pressure range between  $(1-3) \times$ 10<sup>-8</sup> Torr. The binding energies for all spectra were referenced to the adventitious C 1s core level at 284.6 eV. The spectra were deconvoluted using CasaXPS, a commercially available XPS analysis program. The Mo  $3d_{5/2}$  and  $3d_{3/2}$  doublets were fit with a splitting of 3.15 eV and an intensity ratio of 3:2. X-ray absorption spectroscopy experiments were performed at the 10-ID-B beamline of the Advanced Photon Source, Argonne National Laboratory. NP-MoC<sub>1-x</sub>/C (3.66 wt % Mo) were loaded into 1 mm outer diameter thin-walled quartz X-ray capillaries and examined in a transmission geometry. Data were collected from 200 eV below the Mo K-edge (20 000 eV) to ~1000 eV above the edge. Data processing and subsequent extended X-ray absorption fine-structure (EXAFS) modeling were performed with the Demeter XAS software package. Models were constructed using Mo-C and Mo-Mo scattering paths from a known Mo carbide crystal structure.<sup>28</sup> A Mo foil was used to obtain a  $S_0^2$  of 0.843 for all EXAFS models. High-energy X-ray total scattering experiments were performed at the 11-ID-B beamline of the Advanced Photon Source, Argonne National Laboratory, using an Xray energy of 86.7 keV. A sample to detector distance of 300 mm was used to reach  $\sim 37$  Å<sup>-1</sup>. Atomic pair distribution functions (PDFs) were generated using the program RAD.<sup>29</sup> Differential PDF methods to obtain the  $MoC_{1-x}$  PDFs by subtracting the carbon support PDF from the  $MoC_{1-x}$  PDFs, as previously described.<sup>30</sup> Theoretical PDFs of reference Mo-containing crystal structures were calculated in PDFgui<sup>31</sup> using published crystal structure data. <sup>28,32–35</sup> Nanoparticle models were generated using reverse Monte Carlo (RMC) simulations using the RMC++ program.<sup>36</sup> Starting configurations were built from the known bulk lattice of  $MoC_{1-x}^{28}$  with a size of 2.2 nm, which is the representative size observed in TEM. RMC simulations were performed with coordination number constraints obtained from EXAFS modeling to create experimentally accurate models that are not driven explicitly due to entropic effects. Structure models from RMC are presented using Mercury 4.0 visualization software.<sup>37</sup> Catalytic site densities were determined by carbon monoxide (CO) chemisorption at 50 °C over the pressure range of 13-60 kPa using a quantachrome Autosorb 1-C. Samples (120-300 mg) were reduced with flowing UHP  $H_2$  at 450 °C for 2 h (bulk  $\alpha$ - $MoC_{1-x}$  and  $NP-MoC_{1-x}/C$ ) or 400 °C for 2 h (Fe/ $\gamma$ -Al<sub>2</sub>O<sub>3</sub>), followed by evacuation at the reduction temperature for 2 h. The CO\*-site density (units of  $\mu mol_{CO^*}/g_{cat}$ ) was determined from the difference of the combined and weak isotherms extrapolated to zero pressure.

Catalytic CO<sub>2</sub> Hydrogenation. Catalytic activities of bulk molybdenum carbide materials (i.e., bulk  $\alpha$ -MoC<sub>1-x</sub>), carbonsupported molybdenum carbide nanoparticles (NP-MoC $_{1-x}/C$ ), and 14.4% Fe/ $\gamma$ -Al<sub>2</sub>O<sub>3</sub> were evaluated for the CO<sub>2</sub> hydrogenation reaction in a 1 in. ID fixed bed stainless steel reactor. In a typical experiment with bulk  $\alpha$ -MoC<sub>1-x</sub> catalyst, ca. 0.1 g of catalyst (150–300  $\mu$ m particle size) was diluted with SiC (250-524  $\mu$ m in particle size) with a 1:1 volume ratio to enhance heat transfer. In reactions with the NP- $MoC_{1-x}/C$  catalyst, ca. 0.9 g of catalyst was used without any diluent. The catalyst was pretreated under 95% H<sub>2</sub>/5% Ar flow (50 sccm) at either 400 °C (for Fe/ $\gamma$ -Al<sub>2</sub>O<sub>3</sub>) or 450 °C (for the MoC<sub>1-x</sub> catalysts) for 2 h. The reactions with MoC<sub>1-x</sub> catalysts were performed at 300 °C and 2 MPa, with feed gas composition of 26:70:4 mol % for CO<sub>2</sub>:H<sub>2</sub>:Ar, respectively (corresponding to a molar H<sub>2</sub>:CO<sub>2</sub> ratio in the feed of 2.7). The reactant flow rate was controlled to achieve the

same weight-hourly space velocity (WHSV) of ca. 40  $\ensuremath{h^{-1}}$  based on active metal component (i.e., Mo). The reaction conditions for the conventional supported Fe/γ-Al<sub>2</sub>O<sub>3</sub> catalyst were similar to those in previous reports. 38,39 The catalyst (ca. 1 g) was pretreated at 400 °C for 2 h, and the reaction was performed at 300 °C, 1.1 MPa with feed gas composition of 24:72:4 mol % for CO<sub>2</sub>:H<sub>2</sub>:Ar, respectively, with a WHSV of 10 h<sup>-1</sup> based on Fe (total gas hourly space velocity (GHSV) of 3600 mL/g/h). Product analysis was performed online by an Agilent Technologies 7890B gas chromatograph equipped with flame ionization detectors (FIDs) and a thermal conductivity detector (TCD). The concentration of each compound was quantified by correlating its peak area with the response factor obtained from calibration standards. Sampling of the inlet stream was also performed when the reactant flow was started to measure concentration of the feed stream until it stabilized. Conversion was calculated as  $\Sigma$ (molar flow rate of C in all products)/(molar flow rate of inlet CO<sub>2</sub>). The Cselectivity of product i was calculated as (molar flow rate of C in product  $(i)/\Sigma$  (molar flow rate of C in all products). Total site-time yield (STY) was calculated as  $\Sigma$ (moles of C in all products)/(moles of CO adsorption site)/h. Site-time yield for C2+ products was calculated as  $\Sigma$ (moles of C in  $C_{2+}$  products)/(moles of CO adsorption site)/h.

#### ■ RESULTS AND DISCUSSION

**Synthesis of NP-MoC**<sub>1-x</sub>. Molybdenum hexacarbonyl was identified as a promising source of air-stable, low-valent Mo for preparing Mo carbide due to its stability, preformed Mo-C bonds, and low cost. Early reports 40,411 determined that Mo(CO)<sub>6</sub> may be pyrolyzed at relatively low temperatures (300-475 °C) under vacuum with partial pressures of CO or H<sub>2</sub> between 0.02–0.2 Torr to form face-centered cubic (fcc)  $\alpha$ -MoC<sub>1-x</sub> or structurally analogous oxycarbides (MoC<sub>0.34</sub>O<sub>0.31</sub>), respectively. These reports indicate two critical properties of the Mo(CO)<sub>6</sub> precursor that make it suitable for the solution-phase synthesis of Mo carbide under mild conditions: (1) it may be readily decomposed in the absence of additional sources of reactive carbon to form carbidic phases, and (2) the decomposition temperature range (300-475 °C) is within the typical working temperatures of solutionphase NP synthesis using high-boiling solvents. Exploiting these physical properties, we developed a facile small-scale batch synthesis to prepare  $NP-MoC_{1-x}$  via the thermolytic decomposition of Mo(CO)<sub>6</sub> in the presence of oleylamine (OAm) and 1-octadecene. The Mo(CO)<sub>6</sub> precursor remains insoluble until around 100 °C and readily sublimes in the neck of the reaction flask, leading to a moderate yield of NP- $MoC_{1-x}$  in the batch synthesis (ca. 40–50%). Above 100 °C, a homogeneous yellow solution is obtained that progressively transitions to an orange-red solution as the temperature nears ca. 200 °C, implicating the formation of a Mo(CO)<sub>4</sub>(OAm)<sub>2</sub> species as Mo(CO)<sub>6</sub> readily reacts with amines and imines to form disubstituted Mo(CO)<sub>4</sub>L<sub>2</sub> complexes under similar conditions. 42 At ca. 240 °C, the Mo-precursor complex begins to decompose, and over the course of the 1 h reaction time at 300 °C, forms phase-pure and highly dispersible NPs of  $\alpha$ - $MoC_{1-x}$  (Figure S1a). We found that this metal-carbonylbased synthesis approach could be readily extended to other metal carbide NPs such as  $\beta$ -WC using W(CO)<sub>6</sub> (Figure S1b,c). Details of the batch synthesis method can be found in the Supporting Information. Despite providing a mild route to dispersible  $\alpha$ -MoC<sub>1-x</sub> NPs, this traditional batch approach has disadvantages that may limit industrial applicability including the small production scale and low throughput inherent in batch reactions, as well as the low yield of NPs as a result of the sublimation of the  $Mo(CO)_6$  precursor.

Journal of the American Chemical Society

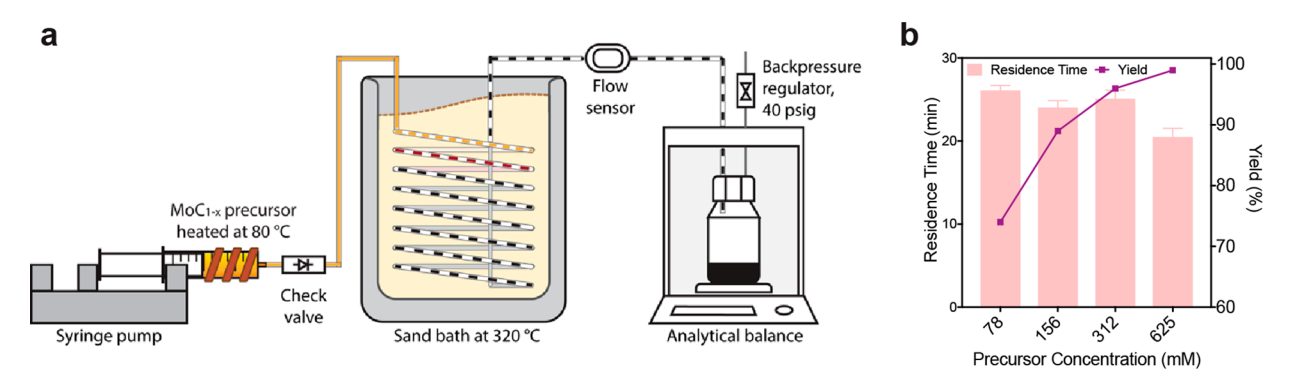
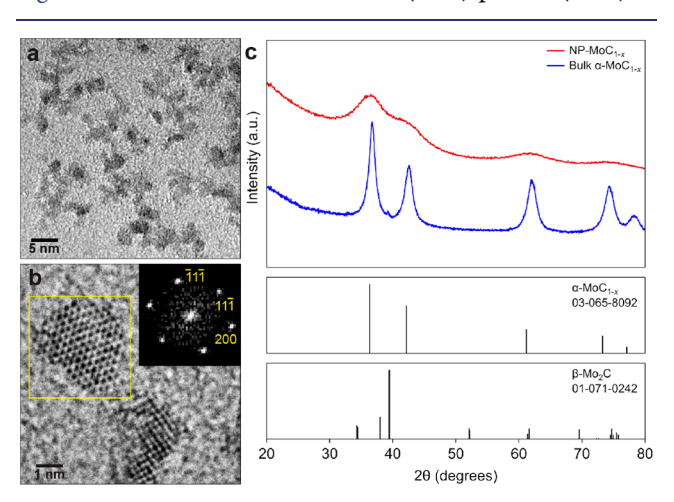


Figure 1. (a) Representation of the millifluidic reactor system for the continuous flow synthesis of NP-MoC<sub>1-x</sub> and (b) reaction residence time and NP-MoC<sub>1-x</sub> product yield as a function of  $[Mo(CO)_6]$ .

To circumvent the issues inherent with the small-scale batch synthesis and enable the high throughput required for catalytic evaluation of the resulting NPs, we developed a continuous millifluidic (mF) process to execute the thermolytic decomposition of Mo(CO)<sub>6</sub> under conditions similar to those of the batch synthesis. The continuous mF synthesis of NP-MoC<sub>1-x</sub> was performed using the reactor configuration illustrated in Figure 1a. Briefly, a preheated Mo(CO)<sub>6</sub> precursor solution was injected at a constant flow rate of 12 mL h<sup>-1</sup> into a borosilicate mF reactor (ID = 1.8 mm) heated to 320 °C. Upon heating to the reaction temperature, the Mo(CO)<sub>6</sub> precursor decomposed, liberating CO and separating the liquid phase into isolated plugs in the reactor channel. The system was fitted with a check valve upstream of the heated reactor to prevent the backflow of precursor solution caused by gas evolution during precursor decomposition. In addition, the mF reactor was operated at 40 psig to further suppress in situ gas evolution and maintain longer and more consistent residence times. As the reaction mixture passed through the outlet of the heated segment of the reactor, the reaction was rapidly thermally quenched as heat dissipated from the narrow diameter reaction channel upon exposure to ambient temperature air. Synthetic throughput was optimized by increasing the precursor concentration 8-fold from 78 mM (from batch reaction) to 625 mM, and analysis by X-ray diffraction (XRD, Figure S2) and transmission electron microscopy (TEM, Figure S3a-d) demonstrated consistent particle morphology and crystallinity that were analogous to those of the small-scale batch product. Following synthesis, the  $MoC_{1-x}$  NPs were dispersed on a high-surface area carbon, achieving a loading of 3.66 wt % Mo for the NP-MoC<sub>1-x</sub>/C. Over the concentration range from 78 to 312 mM (with a fixed OAm:Mo ratio of 4), it was observed that the residence time as determined by a dissipation flow sensor (Figure S4) remained nearly constant; however, there was a significant decrease in the residence time (Figure 1b) for the highest precursor concentration (625 mM) resulting from increased gas evolution. The NP-MoC<sub>1-x</sub> product yields as determined by thermogravimetric analysis for Mo(CO)<sub>6</sub> precursor concentrations of 78, 156, 312, and 625 mM were 74%, 89%, 96%, and 99%, respectively, demonstrating near quantitative yields of NP-MoC<sub>1-x</sub> using this mF synthesis approach. This represents a significant improvement in throughput over the small-scale batch reaction, with higher precursor concentrations (625 vs 78 mM), reduced reaction times (20 min vs 1 h), and greater yields (99% vs 40-50%), and translates to a single-channel reactor throughput of NP-MoC<sub>1-x</sub> of 18.6 g per 24 h of reactor

operation, equating to >450 g of  $\sim$ 4 wt % supported NP-MoC $_{1-x}$  catalyst.

**Structural Characterization of NP-MoC**<sub>1-x</sub>. All further characterization was performed on the NP-MoC<sub>1-x</sub> produced from the optimized mF synthesis conditions (i.e., 625 mM precursor concentration) and the carbon supported material (NP-MoC<sub>1-x</sub>/C) where noted. The resulting MoC<sub>1-x</sub> NPs were found to be crystalline with a multipodal morphology and an approximate crystallite size of  $2.2 \pm 0.4$  nm, as shown in Figure 2a. The fast Fourier transform (FFT) pattern (inset) of



**Figure 2.** (a) TEM image of α-MoC $_{1-x}$  NPs showing multipodal morphology and (b) high-resolution TEM image with FFT pattern (inset) of outlined region indexed to the [011] zone axis. (c) XRD patterns for NP-MoC $_{1-x}$  and bulk α-MoC $_{1-x}$  with corresponding reference patterns.

the selected region in Figure 2b can be indexed to the [011] zone axis of fcc  $\alpha$ -MoC<sub>1-x</sub>, with measured lattice spacings of 0.21 nm assigned to the (200) planes and 0.24 and 0.25 nm to the (111) planes, in agreement with previous reports. He XRD pattern of the unsupported NP-MoC<sub>1-x</sub>, shown in Figure 2c, corresponds well with the bulk  $\alpha$ -MoC<sub>1-x</sub> diffraction pattern and the ICDD powder diffraction file 03-065-8092, without additional reflections associated with any other crystalline carbide, oxide, or metallic phases. The XRD pattern of bulk  $\alpha$ -MoC<sub>1-x</sub> synthesized as previously reported is presented in Figure 2c and was found to be predominantly the  $\alpha$ -MoC<sub>1-x</sub> phase (>99.5% by single-peak reference intensity ratio analysis) with trace  $\beta$ -Mo<sub>2</sub>C present, which can be observed from the topotactic synthesis of the fcc  $\alpha$ -MoC<sub>1-x</sub> phase. Scherrer analysis of the (111) diffraction peak for the

Journal of the American Chemical Society

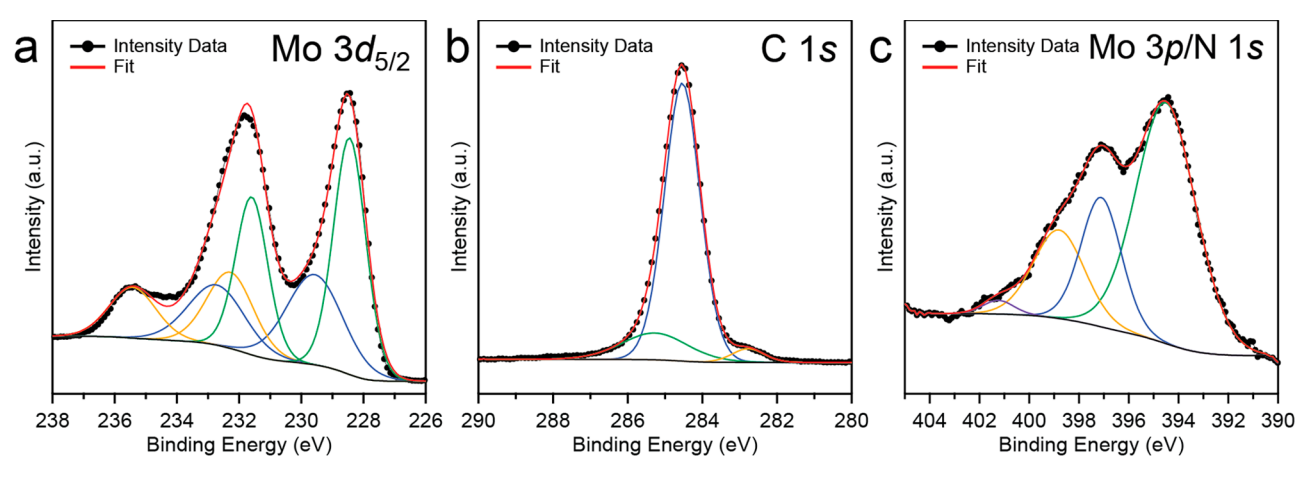


Figure 3. High-resolution (a) Mo 3d, (b) C 1s, and (c) Mo 3p/N 1s XPS spectra for  $\alpha$ -MoC<sub>1-x</sub> NPs prepared in flow using a 625 mM precursor solution.

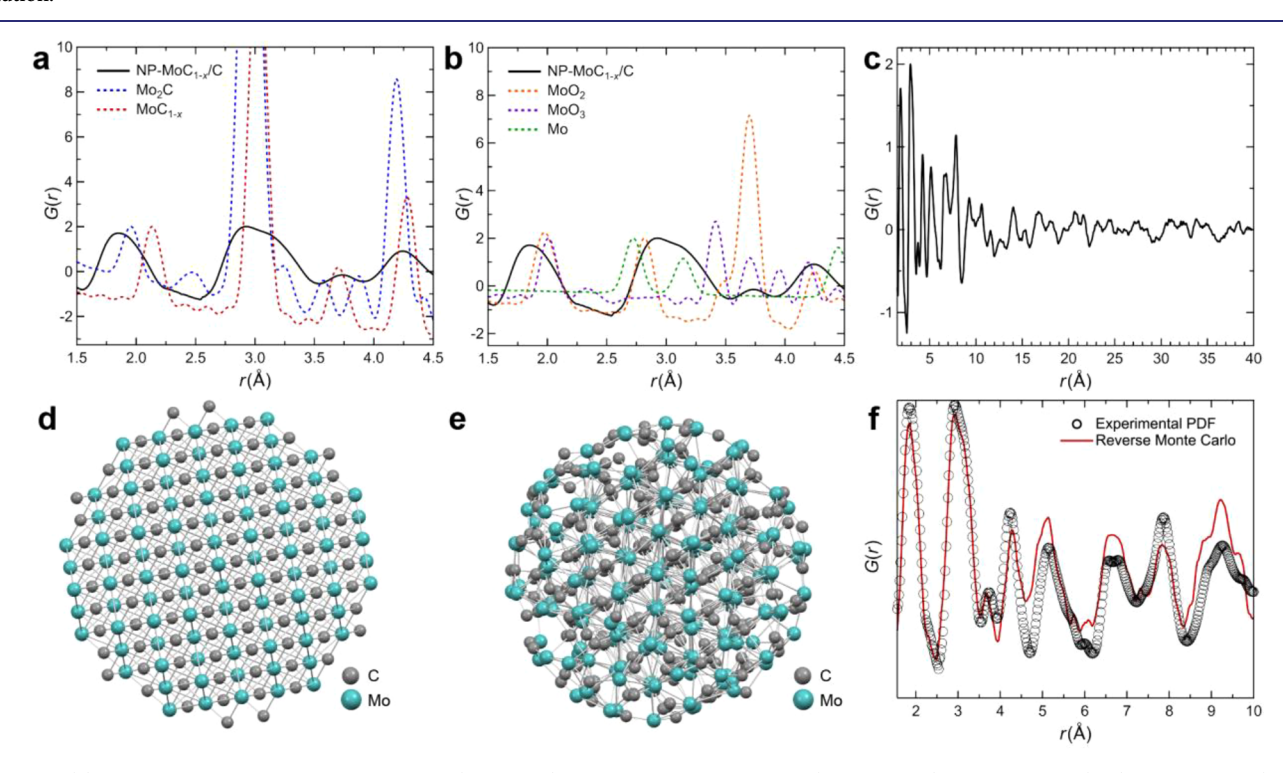


Figure 4. (a) Experimental PDF for NP-MoC $_{1-x}$ /C (black line) as well as calculated PDFs (dashed lines) for α-MoC $_{1-x}$  (red) and β-Mo $_2$ C (blue). (b) Experimental PDF for NP-MoC $_{1-x}$ /C (black line) and calculated PDFs (dashed lines) for Mo(0) (green), MoO $_2$  (red), and MoO $_3$  (blue). (c) Atomic PDF of NP-MoC $_{1-x}$ /C and (d) the fcc MoC $_{1-x}$  starting configuration, (e) RMC-generated NP configuration of MoC $_{1-x}$ , and (f) RMC fit of the NP-MoC $_{1-x}$  data.

 $NP-MoC_{1-x}$  gives a crystallite size of 1.3 nm, which is in good agreement with the diameter of the crystallites observed by TEM.

The unsupported  $MoC_{1-x}$  NPs were further investigated using X-ray photoelectron spectroscopy (XPS), where qualitative peak fitting was performed to help assign binding energies. The deconvoluted high-resolution Mo 3d XPS spectrum (Figure 3a) exhibited three sets of Mo  $3d_{5/2}$  doublets consistent with a range of oxidation states for Mo from +2 to +6. The doublet observed at 228.4 eV can be assigned to  $Mo^{2+}$  in  $\alpha$ -MoC<sub>1-x</sub>. The feature at 229.8 eV is consistent with the presence of  $Mo^{4+}$  species,  $Mo^{4+}$  while the signal at 232.1 eV can be assigned to oxidized  $Mo^{6+}$  species by XPS suggests the  $\alpha$ -MoC<sub>1-x</sub> NPs contain oxidized species, such as surface Mo sites with

Mo–O bonds, similar to those observed for passivated bulk carbides. However, the  $\mathrm{MoC_{1-x}}$  NPs exhibit no bulk oxidation after handling in air as-synthesized, which is noted by the absence of any features associated with  $\mathrm{MoO_2}$  and  $\mathrm{MoO_3}$  in the XRD pattern (Figure 2c). This is in contrast to the bulk Mo carbides, which require passivation with low concentrations of  $\mathrm{O_2}$  to prevent uncontrolled bulk oxidation. The high-resolution C 1s envelope (Figure 3b) confirms the presence of carbidic carbon with a characteristic peak at 282.8 eV. There is also a large feature associated with adventitious carbon originating from the presence of organic surfactants at 284.5 eV as well as a smaller peak associated with adsorbed carbon oxides at 285.4 eV. The overlapping Mo 3p<sub>3/2</sub> and N 1s region was deconvoluted by constraining the observed Mo 3p<sub>3/2</sub> doublet from the N 1s peaks using the known separation

energy and ratio of intensity (2:1). The peak at a binding energy of 394.5 eV (Figure 3c) can be attributed to carbidic Mo<sup>2+,52</sup> The peak observed at 396.9 eV can be attributed to the presence of oleylimine groups resulting from the oxidation of oleylamine. This is in good agreement with the FT-IR spectrum of the  $MoC_{1-x}$  NPs (Figure S6) that exhibit a feature at ca. 1634 cm<sup>-1</sup> that can be ascribed to a -C=N stretch.<sup>53</sup> The peaks observed by XPS at 399.0 and 401.1 eV are consistent with the presence of oleylamine (-NH<sub>2</sub>) and oleylammonium (-NH<sub>3</sub><sup>+</sup>), respectively (Figure 3c).<sup>54</sup> Furthermore, the FT-IR spectrum displayed clear bands in the range of 2850-2955 cm<sup>-1</sup> corresponding to symmetric and asymmetric stretching vibrations of -CH<sub>2</sub>- and -CH<sub>3</sub> species  $\nu(C-H)$ , additionally confirming the presence of organic oleylligands (Figure S6). The band associated with  $\nu(N-H)$  is observed at 3203 cm<sup>-1</sup> and is broadened and shifted to a lower wavenumber as compared to free oleylamine (3321 cm<sup>-1</sup>), which is typical for ligand coordination to an NP surface. <sup>56,57</sup>

Atomic pair distribution function (PDF) analysis was used to provide greater insight into the structure of the small  $MoC_{1-x}$  NPs by comparison to structures with real-space distances. Atomic PDFs are the Fourier transform of the total scattering pattern (both Bragg and diffuse features) taken at sufficiently high reciprocal space vectors (>ca. 20  $\text{Å}^{-1}$ ) into atomic pair distances. The more immediate intuitive structural understanding of real-space distances and the ability to probe disordered materials are particularly well suited for characterizing the atomic-scale structure of NPs and have previously been used to determine the structure of encapsulated MoC<sub>x</sub> nanoclusters within zeolite pores.<sup>60</sup> The PDF of carbon supported MoC<sub>1-x</sub> NPs is shown in Figure 4a,b along with the calculated PDFs of fcc  $\alpha$ -MoC<sub>1-x</sub>, orthorhombic  $\beta$ -Mo<sub>2</sub>C, <sup>32</sup> body-centered cubic Mo(0), <sup>33</sup> MoO<sub>2</sub>, <sup>34</sup> and MoO<sub>3</sub>. The NP-MoC<sub>1-x</sub>/C exhibited broad atom pair peaks that rapidly oscillate to zero before 20 Å (Figure 4c). This observation is consistent with the absence of long-range ordering and the small size of the NPs as revealed by their broad Bragg-like features and the size of the crystalline domains observed by XRD and TEM. PDF analysis reveals that the structure of the  $MoC_{1-x}$  NPs most closely resembles that of bulk  $\alpha$ -MoC<sub>1-x</sub> or  $\beta$ -Mo<sub>2</sub>C, with minimal relationship to Mo, MoO<sub>2</sub>, or MoO<sub>3</sub> over the length scale of ca. 3.5 Å, and the first coordination sphere representing Mo-C atomic pairs at 1.89 Å. This Mo-C atomic pair distance is contracted as compared to the distances for bulk  $\alpha$ -MoC<sub>1-x</sub> (2.14 Å) and bulk  $\beta$ -Mo<sub>2</sub>C (1.94 Å), which is not uncommon in disordered nanoscale materials. 61 It is important to note that the breadth of the feature attributed to the first coordination sphere suggests contributions from coordinated surface species (i.e., stabilizing ligands) coupled with the lack of long-range ordering characteristic of small NPs (i.e., ca. ≤2 nm).<sup>62-</sup> The feature representing the second coordination sphere of Mo-Mo distances (and to a lesser extent C-C distances) appears to be a superposition of two features, with maxima at 2.90 and 3.1 Å. This broad Mo-Mo peak observed for NP-MoC<sub>1-x</sub>/C encompasses the expected Mo-Mo distances of both bulk  $\alpha$ -MoC<sub>1-x</sub> and  $\beta$ -Mo<sub>2</sub>C, further indicating atypical local ordering. The absence of distinct correlation peaks at r =4.5, 3.7, and 3.4 Å corresponding to Mo(0),  $MoO_2$ , and  $MoO_3$ , respectively, indicates that any of these species present in the sample are of lower contribution to the PDF than the dominant carbide phase.

X-ray absorption spectroscopy (XAS) experiments were performed to complement the PDF analysis in determining the local structure of the Mo atoms in the  $MoC_{1-x}$  NPs. The features and  $E_0$  value of 20 013 eV observed in the X-ray absorption near-edge spectrum (XANES), shown in Figure S7a,b, are in good agreement with previously reported data for bulk  $\alpha$ -MoC<sub>1-x</sub>, strongly suggesting the majority of the Mo atoms exhibit an immediate local symmetry and oxidation state consistent with the bulk lattice. The extended X-ray absorption fine-structure spectra (EXAFS) were obtained after background normalization to remove any contributions from the carbon support,  $k^2$  weighting, and Fourier transformation of the XAS data past the Mo K-edge (Figure S7c). The EXAFS spectrum of the NP-MoC<sub>1-x</sub>/C material exhibits features at 1.56 and 2.60 Å (not corrected for phase shift) for the Mo-C and Mo-Mo coordination spheres, respectively. EXAFS modeling (Figure S7d-f) provides quantitative evidence of reduced order, as summarized in Table S1. The Mo-C coordination number (CN) for NP-MoC<sub>1-x</sub>/C (5.22  $\pm$  0.28) and the Mo–Mo CN (3.48  $\pm$  0.52) are significantly lower than the CNs for bulk  $\alpha\text{-MoC}_{1-x}$  (6.0 and 12.0, respectively) and are a further indicator of structural disorder in the NP- $MoC_{1-r}/C$  material.

The local structural information from EXAFS modeling was used in conjunction with the PDF data to prepare a structure model of an  $MoC_{1-x}$  particle using reverse Monte Carlo (RMC) simulation. RMC modeling is particularly advantageous for disordered nanomaterial systems, as the experimental data are the primary driver for fitting and not crystallographic constraints or theoretical constructs. 66,67 For reference, the starting configuration is shown in Figure 4d. The resulting RMC model shown in Figure 4e illustrates the lack of longrange order and reveals significant surface undercoordination, as expected. The RMC-generated PDF fits the experimental data with an agreement factor (R<sub>w</sub>) below 5% as shown in Figure 4f. In particular, many of the Mo atoms (teal) are significantly distorted from the crystallographic conditions, which RMC generates to satisfy the lack of order with the PDF and the significantly reduced Mo-Mo distances from the EXAFs modeling. For comparison purposes, Table S1 summarizes key identifying structural features for NP- $MoC_{1-r}/C$  as compared to the bulk lattice. Mo-C CNs of NP-MoC<sub>1-x</sub>/C were derived from EXAFS modeling and closely reproduced by the RMC model and are lower than those found in the bulk lattice (ca. 5 as compared to 6). Additionally, the Mo-Mo CN of 3.48 is significantly lower than the bulk values of 12, suggesting that the small polycrystalline NPs are composed of disordered clusters of Mo and C atoms. A decrease in the nearest neighbor distance of the first coordination sphere of Mo-Mo atoms from 3.026 for bulk  $\alpha$ -MoC<sub>1-x</sub> as compared to 2.88 for the nanoscale analogue further suggests a disordered nanoscale phenomenon of these materials, as shortened distances are readily observed from the PDF data.

**CO<sub>2</sub> Hydrogenation.** To assess the impact of nanostructuring on the catalytic performance of  $MoC_{1-x}$  catalytic  $CO_2$  hydrogenation reactions were performed over the carbon-supported  $MoC_{1-x}$  NPs and compared to a traditionally synthesized bulk  $\alpha$ -Mo $C_{1-x}$  catalyst in a continuous-flow fixed bed reactor. The reaction conditions employed in this study were 2 MPa, 300 °C, and a  $H_2$ : $CO_2$  ratio of 2.7, as informed from recent reports evaluating  $CO_2$  hydrogenation over bulk  $\beta$ -Mo<sub>2</sub>C.  $^{68-71}$  A weight-hourly space velocity (WHSV) of 40 h<sup>-1</sup>

Journal of the American Chemical Society

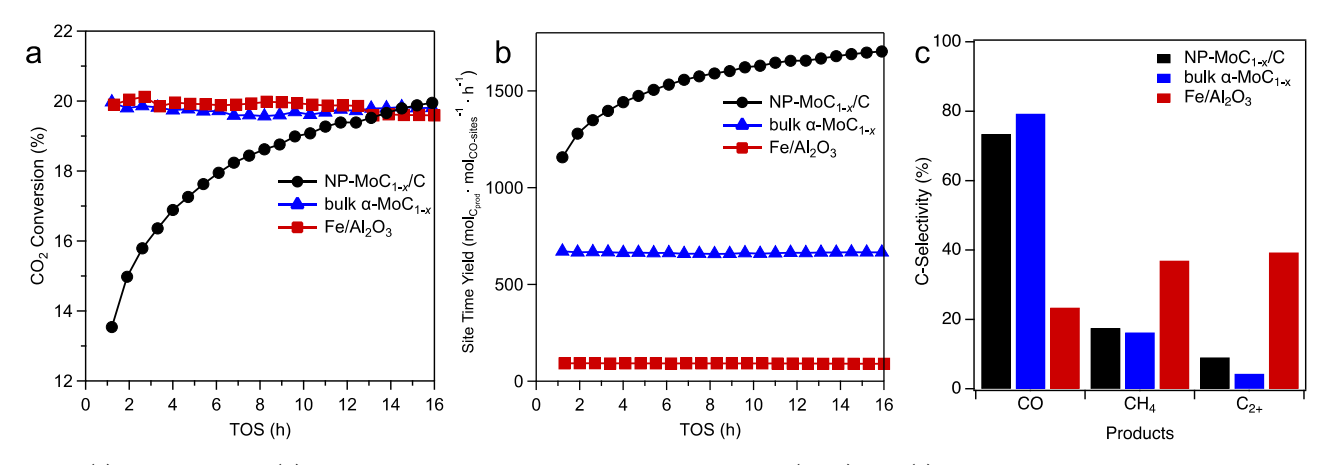


Figure 5. (a) Conversion and (b) total site-time yields as a function of time on stream (TOS), and (c) product carbon selectivity at 14–16 h TOS for CO<sub>2</sub> hydrogenation over NP-MoC<sub>1-x</sub>/C, bulk  $\alpha$ -MoC<sub>1-x</sub>, and Fe/γ-Al<sub>2</sub>O<sub>3</sub> catalysts. Reaction conditions: 2 MPa, 300 °C, H<sub>2</sub>:CO<sub>2</sub> = 2.7, and WHSV = 40 h<sup>-1</sup> for MoC<sub>1-x</sub> catalysts; 300 °C, 1.1 MPa, H<sub>2</sub>:CO<sub>2</sub> = 3, and WHSV = 10 h<sup>-1</sup> for Fe/γ-Al<sub>2</sub>O<sub>3</sub> catalyst. Data in panel c are a comparison at comparable conversion values of 19.6–19.8% for all three catalysts, and the standard deviation in selectivity for all catalysts was <0.2%.

on a gravimetric Mo basis (as determined by inductively coupled plasma optical emission spectroscopy; Table S2) was employed here for the carbide catalysts. A traditional CO2 Fischer-Tropsch synthesis (FTS) catalyst (Fe/γ-Al<sub>2</sub>O<sub>3</sub>, 14.4 wt % Fe) was also synthesized as previously reported and evaluated to benchmark the performance of the carbide catalysts. 38,39 Lower pressure conditions and a lower WHSV were employed for the  $Fe/\gamma$ -Al<sub>2</sub>O<sub>3</sub> catalyst to match literature reports (1.1 MPa, 300 °C,  $H_2$ : $CO_2$  = 3, WHSV of 10  $h^{-1}$  based on gravimetric Fe content). 38,39 Comparable performance of the Fe/ $\gamma$ -Al<sub>2</sub>O<sub>3</sub> catalyst was observed at the same pressure and temperature conditions under which the  $MoC_{1-x}$  catalysts were operated (Table S2). The CO2 conversions for the bulk  $\alpha$ -MoC<sub>1-x</sub>, NP-MoC<sub>1-x</sub>/C, and benchmark Fe/ $\gamma$ -Al<sub>2</sub>O<sub>3</sub> catalysts as a function of time on stream (TOS) are presented in Figure 5a. The bulk  $\alpha$ -MoC<sub>1-x</sub> and benchmark Fe/ $\gamma$ -Al<sub>2</sub>O<sub>3</sub> catalysts exhibited stable conversion throughout the testing period (16 h TOS). In contrast, the NP-MoC<sub>1-x</sub>/C catalyst demonstrated an induction period where conversion increased from 13.5% to 20.0% over the same time period. This induction period was observed for the NP-MoC<sub>1-r</sub>/C catalyst irrespective of the duration of H2 pretreatment, which was varied from 2 to 12 h, suggesting any restructuring that may be responsible for this catalytic behavior is caused during reaction. This is further supported by ambient pressure in situ XRD experiments in flowing H2 at 450 °C that revealed no bulk structural changes to the NP-MoC $_{1-x}/C$  catalyst during a 2 h reduction (Figure S8a). However, upon introduction of CO<sub>2</sub> at 300 °C, the reflections associated with the  $\alpha$ -MoC<sub>1-x</sub> phase decreased with exposure with a concomitant increase in the broad carbon background centered at ca. 24.8°  $2\theta$ . There is no evidence of any other crystalline carbide, oxide, or metallic phases forming, suggesting this decrease in intensity could be related to carbon deposition resulting from reaction with CO2 and/or a loss of crystallinity of the  $MoC_{1-x}$  particles during reaction. After ca. 13 h TOS, CO2 conversion over the NP-MoC<sub>1-x</sub>/C catalyst reached parity with the bulk carbides and benchmark Fe/γ-Al<sub>2</sub>O<sub>3</sub> catalysts at 19.5%. Catalyst activity was normalized to CO-binding site density as measured by CO chemisorption (Table S2) to give site-time yield (STY) values. Despite the induction period, the NP-MoC<sub>1-x</sub>/C catalyst demonstrated a significantly greater STY than both the bulk  $\alpha$ - $MoC_{1-x}$  and  $Fe/\gamma$ -Al<sub>2</sub>O<sub>3</sub> catalysts (Figure 5b). At comparable

conversion values of 19.6–19.8% (14–16 h TOS), the STY of the NP-MoC $_{1-x}$ /C catalyst (1695 mol $_{\text{C-prod}}$  mol $^{-1}_{\text{CO-site}}$  h $^{-1}$ ) was 2.5-fold greater than that of the bulk  $\alpha$ -MoC $_{1-x}$  (666 mol $_{\text{C-prod}}$  mol $^{-1}_{\text{CO-site}}$  h $^{-1}$ ) and 19-fold greater than that of the benchmark Fe/ $\gamma$ -Al $_2$ O $_3$  catalyst (91 mol $_{\text{C-prod}}$  mol $^{-1}_{\text{CO-site}}$  h $^{-1}$ , Table S2). The increased STY observed for the NP-MoC $_{1-x}$ /C catalyst may be attributed to the significant surface undercoordination revealed by the EXAFS modeling and RMC simulation and exemplifies the catalytic performance improvements that are attainable through the controlled synthesis of TMC NPs. Moreover, the MoC $_{1-x}$ /C benefits from a significantly greater surface-area-to-volume ratio, where, in this case, a catalyst with 3.66 wt % Mo outperformed the bulk analogue due to improved Mo utilization.

The product carbon-selectivities over the NP-MoC<sub>1-x</sub>/C, bulk  $\alpha$ -MoC<sub>1-x</sub>, and benchmark Fe/ $\gamma$ -Al<sub>2</sub>O<sub>3</sub> catalysts are presented in Figure 5c at comparable CO<sub>2</sub> conversions (19.6-19.8%, 14-16 h TOS). A shift in selectivity over the NP- $MoC_{1-x}/C$  material was observed as a function of TOS and conversion (i.e., through the induction period, Figure S9a,b), resulting in increased selectivity to C2+ hydrocarbon products from 6.1% to 9.1% and a concomitant decrease in CO selectivity from 77.3% to 73.4%. This shift in selectivity is attributed to increasing FTS activity through the induction period. The opposite trend was observed over the bulk  $\alpha$ - $MoC_{1-x}$  catalyst, where the selectivity to CO increased from 74.5% to 79.4% and that to C<sub>2+</sub> hydrocarbons decreased from 6.4% to 4.3% with TOS (Figure S9a). This suggests deactivation of the bulk  $\alpha$ -MoC<sub>1-x</sub> catalyst, especially in FTS activity, despite the observation of constant CO<sub>2</sub> conversion over the reaction period. The bulk and NP carbide catalysts exhibited similar selectivity for CH<sub>4</sub> (ca. 16-17%). Unsurprisingly, the NP-MoC $_{1-x}/C$  catalyst, which primarily performed the reverse water-gas shift reaction to form CO, exhibited lower selectivity to  $C_{2+}$  hydrocarbons (6.1–9.1%) as compared to the Fe/ $\gamma$ -Al<sub>2</sub>O<sub>3</sub> catalyst (39.4%), which conducted direct CO2-FT. However, it is important to note that the NP- $MoC_{1-x}/C$  catalyst demonstrated greater  $C_{2+}$  hydrocarbon selectivity than the bulk  $\alpha$ -MoC<sub>1-x</sub> catalyst at all TOS > 2 h and 2-fold greater selectivity to C2+ hydrocarbons than did the bulk  $\alpha$ -MoC<sub>1-x</sub> catalyst at comparable conversions (8.9% vs 4.4%, respectively). When these  $C_{2+}$  selectivity data are considered in the context of site-time yield for  $C_{2+}$  products,

the NP-MoC $_{1-x}/C$  catalyst (152 mol $_{C\text{-prod-C2+}}$  mol $^{-1}_{CO\text{-site}}$  h $^{-1}$ ) greatly outperformed both the bulk  $\alpha\text{-MoC}_{1-x}$  (29 mol $_{C\text{-prod-C2+}}$  mol $^{-1}_{CO\text{-site}}$  h $^{-1}$ ) and the Fe/ $\gamma$ -Al $_2O_3$  (36 mol $_{C\text{-prod-C2+}}$  mol $^{-1}_{CO\text{-site}}$  h $^{-1}$ ) demonstrating the utility in nanostructuring both to tune the product slate and to maximize Mo utilization for the preparation of cost-effective CO $_2$  reduction catalysts.

#### CONCLUSIONS

The solution-phase synthesis strategy presented in this work is a facile and versatile method for preparing nanostructured, stable, and readily dispersible group 6 TMCs. The methods presented herein require no reactive gases or additional thermal treatments to produce phase-pure TMCs, relying instead on the extremely mild thermolytic decomposition of metal-carbonyl precursors. Further, the continuous flow mF approach developed highlights the scalability of this synthetic strategy and demonstrates the feasibility of the production of catalytically relevant quantities of nanostructured TMCs. The resultant dispersible NPs can be deposited on any catalyst support, and, as demonstrated here with the thermocatalytic  $CO_2$  reduction over NP-Mo $C_{1-x}/C$ , their performance on a per-site basis represents a 2-fold improvement as compared to the bulk  $\alpha$ -MoC<sub>1-x</sub> analogue, emphasizing the superior Mo utilization of the nanostructured catalyst. In addition, the increased selectivity toward C2+ products over the NP- $MoC_{1-x}/C$  catalyst highlights the opportunity for the controlled nanostructuring of TMCs to be employed to tune the product slate with the facile synthetic method presented.

## ASSOCIATED CONTENT

### **S** Supporting Information

The Supporting Information is available free of charge at https://pubs.acs.org/doi/10.1021/jacs.9b11238.

Information related to batch synthesis of NP-MoC $_{1-x}$ 0 mF synthesis optimization parameters, FT-IR spectra, and additional TEM, XRD, XAS, and CO $_2$  hydrogenation results (PDF)

## AUTHOR INFORMATION

### **Corresponding Authors**

\*frederick.baddour@nrel.gov

\*brutchey@usc.edu

\*malmstad@usc.edu

#### ORCID ®

Frederick G. Baddour: 0000-0002-5837-5804

Lu Wang: 0000-0002-4136-8261

Daniel A. Ruddy: 0000-0003-2654-3778 Nicholas M. Bedford: 0000-0002-4424-7094 Joshua A. Schaidle: 0000-0003-2189-5678 Richard L. Brutchey: 0000-0002-7781-5596 Noah Malmstadt: 0000-0002-1786-2614

Notes

The authors declare no competing financial interest.

## **■** ACKNOWLEDGMENTS

This research is supported by the U.S. Department of Energy's (DOE) Office of Energy Efficiency and Renewable Energy (EERE) Bioenergy Technologies Office (BETO), under contract DE-AC36-08GO28308 at the National Renewable Energy Laboratory (NREL) in collaboration with the

Chemical Catalysis for Bioenergy Consortium (ChemCatBio), a member of the Energy Materials Network (EMN). This research used the 10-ID-B and 11-ID-B beamlines of the Advanced Photon Source, a U.S. Department of Energy (DOE) Office of Science User Facility operated for the DOE Office of Science by Argonne National Laboratory under contract no. DE-AC02-06CH11357. In addition, 10-ID-B is managed by the Materials Research Collaborative Access Team (MRCAT), which is supported by the Department of Energy and the MRCAT member institutions. We would like to thank Leighanne Gallington at 11-ID-B for experimental support. N.M.B. acknowledges internal support from the Faculty of Engineering at UNSW. R.L.B. and N.M. acknowledge NSF for supporting the mF work under CMMI-1728649. We would like to acknowledge K. Unocic at Oak Ridge National Laboratory for helpful discussions on characterization by electron microscopy and K. T. Ngo at the National Renewable Energy Laboratory for synthetic support. The views expressed in this article do not necessarily represent the views of the U.S. Department of Energy or the United States Government. The U.S. Government retains and the publisher, by accepting the article for publication, acknowledges that the U.S. Government retains a nonexclusive, paid-up, irrevocable, worldwide license to publish or reproduce the published form of this work, or allow others to do so, for U.S. Government purposes.

#### REFERENCES

- (1) Porosoff, M. D.; Yan, B.; Chen, J. G. Catalytic reduction of CO<sub>2</sub> by H<sub>2</sub> for synthesis of CO, methanol and hydrocarbons: challenges and opportunities. *Energy Environ. Sci.* **2016**, 9 (1), 62–73.
- (2) Oyama, S. T. Chapter 1. The Chemistry of Transition Metal Carbides and Nitrides; Springer: Netherland, 1996.
- (3) Lin, Z.; Chen, R.; Qu, Z.; Chen, J. G. Hydrodeoxygenation of biomass-derived oxygenates over metal carbides: from model surfaces to powder catalysts. *Green Chem.* **2018**, *20* (12), 2679–2696.
- (4) Ruddy, D. A.; Schaidle, J. A.; Ferrell, J. R., III; Wang, J.; Moens, L.; Hensley, J. E. Recent advances in heterogeneous catalysts for biooil upgrading via "ex situ catalytic fast pyrolysis": catalyst development through the study of model compounds. *Green Chem.* **2014**, *16* (2), 454–490.
- (5) Nash, C.; Yung, M.; Chen, Y.; Carl, S.; Thompson, L.; Schaidle, J. Catalysis by Metal Carbides and Nitrides. In *Handbook of Solid State Chemistry*; Dronskowski, R., Kikkawa, S., Stein, A., Eds.; Wiley: New York, 2017.
- (6) Tao, A. R.; Habas, S.; Yang, P. Shape Control of Colloidal Metal Nanocrystals. *Small* **2008**, *4* (3), 310–325.
- (7) Leng, Y.; Shao, H.; Wang, Y.; Suzuki, M.; Li, X. A new method to synthesize nickel carbide (Ni<sub>3</sub>C) nanoparticles in solution. *J. Nanosci. Nanotechnol.* **2006**, *6*, 221–226.
- (8) Goto, Y.; Taniguchi, K.; Omata, T.; Otsuka-Yao-Matsuo, S.; Ohashi, N.; Ueda, S.; Yoshikawa, H.; Yamashita, Y.; Oohashi, H.; Kobayashi, K. Formation of Ni<sub>3</sub>C Nanocrystals by Thermolysis of Nickel Acetylacetonate in Oleylamine: Characterization Using Hard X-ray Photoelectron Spectroscopy. *Chem. Mater.* **2008**, *20* (12), 4156–4160.
- (9) Leng, Y.; Liu, Y.; Song, X.; Li, X. Factors Affecting Formation of Metastable Ni<sub>3</sub>C Phase in a Solution-Based Method. *J. Nanosci. Nanotechnol.* **2008**, 8 (9), 4477–4481.
- (10) Schaefer, Z. L.; Weeber, K. M.; Misra, R.; Schiffer, P.; Schaak, R. E. Bridging hcp-Ni and  $Ni_3C$  via a  $Ni_3C_{1-x}$  Solid Solution: Tunable Composition and Magnetism in Colloidal Nickel Carbide Nanoparticles. *Chem. Mater.* **2011**, 23 (9), 2475–2480.
- (11) Meffre, A.; Mehdaoui, B.; Kelsen, V.; Fazzini, P. F.; Carrey, J.; Lachaize, S.; Respaud, M.; Chaudret, B. A Simple Chemical Route toward Monodisperse Iron Carbide Nanoparticles Displaying Tunable

- Magnetic and Unprecedented Hyperthermia Properties. *Nano Lett.* **2012**, 12 (9), 4722–4728.
- (12) Lartigue, L.; Long, J.; Dumail, X.; Nikitenko, S. I.; Cau, C.; Guari, Y.; Stievano, L.; Sougrati, M. T.; Guérin, C.; Sangregorio, C.; Larionova, J. J. J. o. N. R. Iron carbide nanoparticles growth in room temperature ionic liquids [Cn-MIM][BF<sub>4</sub>] (n = 12, 16). *J. Nanopart. Res.* 2013, 15 (4), 1490.
- (13) Yang, C.; Zhao, H.; Hou, Y.; Ma, D.  $Fe_5C_2$  Nanoparticles: A Facile Bromide-Induced Synthesis and as an Active Phase for Fischer—Tropsch Synthesis. *J. Am. Chem. Soc.* **2012**, *134* (38), 15814–15821.
- (14) Yang, Z.; Zhao, T.; Huang, X.; Chu, X.; Tang, T.; Ju, Y.; Wang, Q.; Hou, Y.; Gao, S. Modulating the phases of iron carbide nanoparticles: from a perspective of interfering with the carbon penetration of Fe@Fe<sub>3</sub>O<sub>4</sub> by selectively adsorbed halide ions. *Chemical Science* **2017**, 8 (1), 473–481.
- (15) Hyeon, T.; Fang, M.; Suslick, K. S. Nanostructured Molybdenum Carbide: Sonochemical Synthesis and Catalytic Properties. *J. Am. Chem. Soc.* **1996**, *118* (23), 5492–5493.
- (16) Wu, H. B.; Xia, B. Y.; Yu, L.; Yu, X.-Y.; Lou, X. W. Porous molybdenum carbide nano-octahedrons synthesized via confined carburization in metal-organic frameworks for efficient hydrogen production. *Nat. Commun.* **2015**, *6*, 6512.
- (17) Liang, P.; Gao, H.; Yao, Z.; Jia, R.; Shi, Y.; Sun, Y.; Fan, Q.; Wang, H. Simple synthesis of ultrasmall  $\beta$ -Mo<sub>2</sub>C and  $\alpha$ -MoC<sub>1-x</sub> nanoparticles and new insights into their catalytic mechanisms for dry reforming of methane. *Catal. Sci. Technol.* **2017**, 7 (15), 3312–3324.
- (18) Baddour, F. G.; Nash, C. P.; Schaidle, J. A.; Ruddy, D. A. Synthesis of  $\alpha$ -MoC<sub>1-x</sub> Nanoparticles with a Surface-Modified SBA-15 Hard Template: Determination of Structure–Function Relationships in Acetic Acid Deoxygenation. *Angew. Chem., Int. Ed.* **2016**, 55 (31), 9026–9029.
- (19) Hunt, S. T.; Nimmanwudipong, T.; Román-Leshkov, Y. Engineering Non-sintered, Metal-Terminated Tungsten Carbide Nanoparticles for Catalysis. *Angew. Chem., Int. Ed.* **2014**, 53 (20), 5131–5136.
- (20) Wiles, C.; Watts, P. Continuous flow reactors: a perspective. *Green Chem.* **2012**. *14* (1). 38–54.
- (21) deMello, A. J. Control and detection of chemical reactions in microfluidic systems. *Nature* **2006**, 442, 394–402.
- (22) Roberts, E. J.; Habas, S. E.; Wang, L.; Ruddy, D. A.; White, E. A.; Baddour, F. G.; Griffin, M. B.; Schaidle, J. A.; Malmstadt, N.; Brutchey, R. L. High-Throughput Continuous Flow Synthesis of Nickel Nanoparticles for the Catalytic Hydrodeoxygenation of Guaiacol. ACS Sustainable Chem. Eng. 2017, 5 (1), 632–639.
- (23) Lohse, S. E.; Eller, J. R.; Sivapalan, S. T.; Plews, M. R.; Murphy, C. J. A simple millifluidic benchtop reactor system for the high-throughput synthesis and functionalization of gold nanoparticles with different sizes and shapes. *ACS Nano* **2013**, *7* (5), 4135–4150.
- (24) Kitson, P. J.; Rosnes, M. H.; Sans, V.; Dragone, V.; Cronin, L. Configurable 3D-Printed millifluidic and microfluidic 'lab on a chip' reactionware devices. *Lab Chip* **2012**, *12* (18), 3267–3271.
- (25) Roberts, E. J.; Karadaghi, L. R.; Wang, L.; Malmstadt, N.; Brutchey, R. L. Continuous Flow Methods of Fabricating Catalytically Active Metal Nanoparticles. *ACS Appl. Mater. Interfaces* **2019**, *11* (31), 27479–27502.
- (26) Schneider, C. A.; Rasband, W. S.; Eliceiri, K. W. NIH Image to ImageJ: 25 years of image analysis. *Nat. Methods* **2012**, 9 (7), 671–675.
- (27) Ravel, B.; Newville, M. ATHENA, ARTEMIS, HEPHAESTUS: data analysis for X-ray absorption spectroscopy using IFEFFIT. *J. Synchrotron Radiat.* **2005**, 12 (Pt 4), 537–541.
- (28) Bouchy, C.; Derouane-Abd Hamid, S. B.; Derouane, E. G. A new route to the metastable FCC molybdenum carbide  $\alpha$ -MoC. *Chem. Commun.* **2000**, No. 2, 125–126.
- (29) Petkov, V. RAD, a program for analysis of X-ray diffraction data from amorphous materials for personal computers. *J. Appl. Crystallogr.* **1989**, 22 (4), 387–389.

- (30) Platero-Prats, A. E.; Li, Z.; Gallington, L. C.; Peters, Aaron W.; Hupp, J. T.; Farha, O. K.; Chapman, K. W. Addressing the characterisation challenge to understand catalysis in MOFs: the case of nanoscale Cu supported in NU-1000. *Faraday Discuss.* **2017**, 201 (0), 337–350.
- (31) Farrow, C. L.; Juhas, P.; Liu, J. W.; Bryndin, D.; Bozin, E. S.; Bloch, J.; Proffen, T.; Billinge, S. J. PDFfit2 and PDFgui: computer programs for studying nanostructure in crystals. *J. Phys.: Condens. Matter* **2007**, *19* (33), 335219.
- (32) Parthe, E.; Sadogopan, V. The structure of dimolybdenum carbide by neutron diffraction technique. *Acta Crystallogr.* **1963**, *16* (3), 202–205.
- (33) Bernuy-Lopez, C.; Allix, M.; Bridges, C. A.; Claridge, J. B.; Rosseinsky, M. J.  $Sr_2MgMoO_{6-\delta}$ : Structure, Phase Stability, and Cation Site Order Control of Reduction. *Chem. Mater.* **2007**, *19* (5), 1035–1043.
- (34) Seisenbaeva, G. A.; Sundberg, M.; Nygren, M.; Dubrovinsky, L.; Kessler, V. G. Thermal decomposition of the methoxide complexes  $MoO(OMe)_4$ ,  $Re_4O_6(OMe)_{12}$  and  $(Re_{1-x}Mo_x)O_6(OMe)_{12}$  (0.24  $\leq x \leq$  0.55). *Mater. Chem. Phys.* **2004**, 87 (1), 142–148.
- (35) Braekken, H. Die Kristallstrukturen der Trioxide von Chrom, Molybdaen und Wolfram. Z. Kristallogr. Cryst. Mater. 1931, 78, 484–489.
- (36) Gereben, O.; Pusztai, L. RMC\_POT: A computer code for reverse monte carlo modeling the structure of disordered systems containing molecules of arbitrary complexity. *J. Comput. Chem.* **2012**, 33 (29), 2285–2291.
- (37) Macrae, C. F.; Sovago, I.; Cottrell, S. J.; Galek, P. T. A.; McCabe, P.; Pidcock, E.; Platings, M.; Shields, G. P.; Stevens, J. S.; Towler, M.; Wood, P. A. Mercury 4.0: from visualization to analysis, design and prediction. *J. Appl. Crystallogr.* **2020**, *53* (1), 1–10.
- (38) Satthawong, R.; Koizumi, N.; Song, C.; Prasassarakich, P. Bimetallic Fe-Co catalysts for CO<sub>2</sub> hydrogenation to higher hydrocarbons. *Journal of CO<sub>2</sub> Utilization* **2013**, 3-4, 102-106.
- (39) Satthawong, R.; Koizumi, N.; Song, C.; Prasassarakich, P. Comparative Study on CO<sub>2</sub> Hydrogenation to Higher Hydrocarbons over Fe-Based Bimetallic Catalysts. *Top. Catal.* **2014**, *57* (6), 588–594.
- (40) Lander, J. J.; Germer, L. H. Trans. AIME 1948, 175, 648.
- (41) Ferguson, I. F.; Ainscough, J. B.; Morse, D.; Miller, A. W. Decomposition of Molybdenum Hexacarbonyl. *Nature* **1964**, 202, 1327–1328.
- (42) Stiddard, M. H. B. 910. 2,2'-Bipyridyl derivatives of Group VI carbonyls. *J. Chem. Soc.* **1962**, 0 (0), 4712–4715.
- (43) Yao, S.; Zhang, X.; Zhou, W.; Gao, R.; Xu, W.; Ye, Y.; Lin, L.; Wen, X.; Liu, P.; Chen, B.; Crumlin, E.; Guo, J.; Zuo, Z.; Li, W.; Xie, J.; Lu, L.; Kiely, C. J.; Gu, L.; Shi, C.; Rodriguez, J. A.; Ma, D. Atomic-layered Au clusters on  $\alpha$ -MoC as catalysts for the low-temperature water-gas shift reaction. *Science (Washington, DC, U. S.)* **2017**, 357 (6349), 389–393.
- (44) Volpe, L.; Boudart, M. Compounds of molybdenum and tungsten with high specific surface area: II. Carbides. *J. Solid State Chem.* **1985**, *59* (3), 348–356.
- (45) Gao, J.; Wu, Y.; Jia, C.; Zhong, Z.; Gao, F.; Yang, Y.; Liu, B. Controllable synthesis of  $\alpha$ -MoC<sub>1-x</sub> and  $\beta$ -Mo<sub>2</sub>C nanowires for highly selective CO<sub>2</sub> reduction to CO. *Catal. Commun.* **2016**, 84, 147–150.
- (46) Oshikawa, K.; Nagai, M.; Omi, S. Characterization of Molybdenum Carbides for Methane Reforming by TPR, XRD, and XPS. *J. Phys. Chem. B* **2001**, *105* (38), 9124–9131.
- (47) Torres Galvis, H. M.; Bitter, J. H.; Khare, C. B.; Ruitenbeek, M.; Dugulan, A. I.; de Jong, K. P. Supported iron nanoparticles as catalysts for sustainable production of lower olefins. *Science (Washington, DC, U. S.)* **2012**, 335 (6070), 835–838.
- (48) Cheekatamarla, P. K.; Thomson, W. J. Poisoning effect of thiophene on the catalytic activity of molybdenum carbide during trimethyl pentane reforming for hydrogen generation. *Appl. Catal., A* **2005**, 287 (2), 176–182.
- (49) Delporte, P.; Meunier, F. d. r.; Pham-Huu, C.; Vennegues, P.; Ledoux, M. J.; Guille, J. Physical characterization of molybdenum

- oxycarbide catalyst; TEM, XRD and XPS. Catal. Today 1995, 23 (3), 251–267.
- (50) Choi, J. G.; Thompson, L. T. XPS study of as-prepared and reduced molybdenum oxides. *Appl. Surf. Sci.* 1996, 93 (2), 143–149.
- (51) Wei, Z. B. Z.; Grange, P.; Delmon, B. XPS and XRD studies of fresh and sulfided Mo<sub>2</sub>N. *Appl. Surf. Sci.* **1998**, *135* (1), 107–114.
- (52) Wu, C.; Liu, D.; Li, H.; Li, J. Molybdenum Carbide-Decorated Metallic Cobalt@Nitrogen-Doped Carbon Polyhedrons for Enhanced Electrocatalytic Hydrogen Evolution. *Small* **2018**, *14* (16), 1704227.
- (53) Sreethawong, T.; Shah, K. W.; Zhang, S.-Y.; Ye, E.; Lim, S. H.; Maheswaran, U.; Mao, W. Y.; Han, M.-Y. Optimized production of copper nanostructures with high yields for efficient use as thermal conductivity-enhancing PCM dopant. *J. Mater. Chem. A* **2014**, *2* (10), 3417–3423.
- (54) Socaci, C.; Magerusan, L.; Turcu, R.; Liebscher, J. Developing novel strategies for the functionalization of core—shell magnetic nanoparticles with folic acid derivatives. *Mater. Chem. Phys.* **2015**, *162*, 131–139
- (55) Lu, X.; Tuan, H.-Y.; Chen, J.; Li, Z.-Y.; Korgel, B. A.; Xia, Y. Mechanistic Studies on the Galvanic Replacement Reaction between Multiply Twinned Particles of Ag and HAuCl<sub>4</sub> in an Organic Medium. *J. Am. Chem. Soc.* **2007**, *129* (6), 1733–1742.
- (56) Wang, Z.; Chen, Y.; Zeng, D.; Zhang, Q.; Peng, D.-L. Solution synthesis of triangular and hexagonal nickel nanosheets with the aid of tungsten hexacarbonyl. *CrystEngComm* **2016**, *18* (8), 1295–1301.
- (57) Buchmaier, C.; Rath, T.; Pirolt, F.; Knall, A.-C.; Kaschnitz, P.; Glatter, O.; Wewerka, K.; Hofer, F.; Kunert, B.; Krenn, K.; Trimmel, G. Room temperature synthesis of CuInS<sub>2</sub> nanocrystals. *RSC Adv.* **2016**, *6* (108), 106120–106129.
- (58) Billinge, S. J. L.; Kanatzidis, M. G. Beyond crystallography: the study of disorder, nanocrystallinity and crystallographically challenged materials with pair distribution functions. *Chem. Commun.* **2004**, No. 7, 749–760.
- (59) Petkov, V. Nanostructure by high-energy X-ray diffraction. *Mater. Today* **2008**, *11* (11), 28–38.
- (60) Iida, T.; Shetty, M.; Murugappan, K.; Wang, Z.; Ohara, K.; Wakihara, T.; Román-Leshkov, Y. Encapsulation of Molybdenum Carbide Nanoclusters inside Zeolite Micropores Enables Synergistic Bifunctional Catalysis for Anisole Hydrodeoxygenation. *ACS Catal.* **2017**, *7* (12), 8147–8151.
- (61) Chen, W.-F.; Sasaki, K.; Ma, C.; Frenkel, A. I.; Marinkovic, N.; Muckerman, J. T.; Zhu, Y.; Adzic, R. R. Hydrogen-Evolution Catalysts Based on Non-Noble Metal Nickel—Molybdenum Nitride Nanosheets. *Angew. Chem., Int. Ed.* **2012**, *51* (25), 6131–6135.
- (62) Shi, C.; Redmond, E. L.; Mazaheripour, A.; Juhas, P.; Fuller, T. F.; Billinge, S. J. L. Evidence for Anomalous Bond Softening and Disorder Below 2 nm Diameter in Carbon-Supported Platinum Nanoparticles from the Temperature-Dependent Peak Width of the Atomic Pair Distribution Function. *J. Phys. Chem. C* **2013**, *117* (14), 7226–7230.
- (63) Petkov, V.; Peng, Y.; Williams, G.; Huang, B.; Tomalia, D.; Ren, Y. Structure of gold nanoparticles suspended in water studied by x-ray diffraction and computer simulations. *Phys. Rev. B: Condens. Matter Mater. Phys.* **2005**, 72 (19), 195402–1954028.
- (64) Page, K.; Proffen, T.; Niederberger, M.; Seshadri, R. Probing Local Dipoles and Ligand Structure in BaTiO<sub>3</sub> Nanoparticles. *Chem. Mater.* **2010**, 22 (15), 4386–4391.
- (65) Lee, J. S.; Yie, J. E. An XANES study of carbides of molybdenum and tungsten. *Korean J. Chem. Eng.* **1991**, 8 (3), 164–167
- (66) Keen, D. A.; McGreevy, R. L. Structural modelling of glasses using reverse Monte Carlo simulation. *Nature* **1990**, *344*, 423–425.
- (67) Bedford, N. M.; Ramezani-Dakhel, H.; Slocik, J. M.; Briggs, B. D.; Ren, Y.; Frenkel, A. I.; Petkov, V.; Heinz, H.; Naik, R. R.; Knecht, M. R. Elucidation of Peptide-Directed Palladium Surface Structure for Biologically Tunable Nanocatalysts. *ACS Nano* **2015**, *9* (5), 5082–5092.
- (68) Porosoff, M. D.; Kattel, S.; Li, W.; Liu, P.; Chen, J. G. Identifying trends and descriptors for selective CO<sub>2</sub> conversion to CO

- over transition metal carbides. Chem. Commun. 2015, 51 (32), 6988-6991.
- (69) Porosoff, M. D.; Yang, X.; Boscoboinik, J. A.; Chen, J. G. Molybdenum carbide as alternative catalysts to precious metals for highly selective reduction of CO<sub>2</sub> to CO. *Angew. Chem., Int. Ed.* **2014**, 53 (26), 6705–6709.
- (70) Posada-Pérez, S.; Ramírez, P. J.; Gutiérrez, R. A.; Stacchiola, D. J.; Viñes, F.; Liu, P.; Illas, F.; Rodriguez, J. A. The conversion of  $CO_2$  to methanol on orthorhombic  $\beta$ -Mo<sub>2</sub>C and  $Cu/\beta$ -Mo<sub>2</sub>C catalysts: mechanism for admetal induced change in the selectivity and activity. *Catal. Sci. Technol.* **2016**, 6 (18), 6766–6777.
- (71) Xu, W.; Ramirez, P. J.; Stacchiola, D.; Rodriguez, J. A. J. C. L. Synthesis of  $\alpha$ -MoC<sub>1-x</sub> and  $\beta$ -MoC<sub>y</sub> Catalysts for CO<sub>2</sub> Hydrogenation by Thermal Carburization of Mo-oxide in Hydrocarbon and Hydrogen Mixtures. *Catal. Lett.* **2014**, *144* (8), 1418–1424.